JOURNAL OF THE AMERICAN CHEMICAL SOCIETY

Article

pubs.acs.org/JACS

Structural Evolution of $BaTiO_3$ Nanocrystals Synthesized at Room Temperature

Federico A. Rabuffetti and Richard L. Brutchey*

Department of Chemistry, University of Southern California, Los Angeles, California 90089, United States

Supporting Information

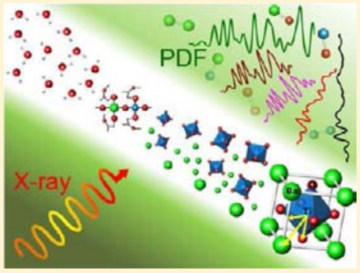

ABSTRACT: Sub-10 nm $BaTiO_3$ nanocrystals were synthesized at room temperature via the vapor diffusion sol−gel method, and their structural evolution during nucleation and growth stages was followed using a series of techniques that probe the atomic structure on different length and time scales. Special emphasis was placed on assessing the evolution of the local symmetry and structural coherence of the resulting nanocrystals, as these are the structural bases for cooperative properties such as ferroelectricity. Although the room-temperature crystal structure of the fully grown nanocrystals appears cubic to Rietveld analysis of synchrotron X-ray diffraction data, Raman spectroscopy and pair distribution function analysis demonstrate the presence of non-centrosymmetric regions arising from the off-centering of the titanium atoms. This finding demonstrates that accounting for diffuse scattering is critical when attempting the structural characterization of nanocrystals with X-ray diffraction. The local symmetry of acentric regions present in $BaTiO_3$ nanocrystals, particularly structural correlations within an individual unit cell *and* between two adjacent unit cells, is best described by a tetragonal *P*4*mm* space group. The orthorhombic *Amm*2 space group also provides an adequate description, suggesting both types of local symmetry can coexist at room temperature. The average magnitude of the local off-center displacements of the titanium atoms along the polar axis is comparable to that observed in bulk $BaTiO_3$, and their coherence length is on the order of 16 Å. The presence of local dipoles suggests that a large amount of macroscopic polarization can be achieved in nanocrystalline $BaTiO_3$ if the coherence of their ferroelectric coupling is further increased.

INTRODUCTION

$BaTiO_3$ (BTO) is one the most technologically relevant eletroceramics. It exhibits a perovskite structure consisting of BaO_{12} cuboctahedra and TiO_6 octahedra. The structure undergoes three temperature-dependent phase transitions: rhombohedral ($R3m$) to orthorhombic ($Amm2$) at −90 °C, orthorhombic to tetragonal ($P4mm$) at 5 °C, and tetragonal to cubic ($Pm\overline{3}m$) at 120 °C;[1] the three low temperature phases exhibit ferroelectric character, whereas the high temperature phase is paraelectric. The microscopic nature of these phase transitions has been exhaustively investigated in single crystal and bulk BTO for over four decades. The long-standing debate of whether the displacive model proposed by Cochran[2] or the eight-site order−disorder model proposed by Bersuker[3] and Comes et al.[4] is better suited to describe the temperature-dependent macroscopic behavior of the system has been the focus of this research effort. Briefly, in the displacive model, the titanium atoms are displaced in the ⟨111⟩, ⟨011⟩, and ⟨001⟩ directions in the rhombohedral, orthorhombic, and tetragonal phases, respectively; in contrast, they sit in the middle of the TiO_6 octahedron in the cubic phase, leading to a centrosymmetric structure. In the eight-site order−disorder model, the titanium atoms are displaced along one of the eight ⟨111⟩ directions in all crystal phases and the correlation between these local displacements changes with temperature. These occur along one, two, four, and eight ⟨111⟩ directions in the rhombohedral, orthorhombic, tetragonal, and cubic phases, respectively. Experimental[5,6] and theoretical[7−11] work carried out in the past decade has reconciled these two apparently contradictory models by demonstrating that both coexist.

The miniaturization of electronic devices has raised the question of how the microscopic structural picture derived for single crystal and bulk forms is affected by strong physical confinement of the material, i.e., the so-called "size effect" in ferroelectrics. Understanding how the local symmetry and structural coherence, which ultimately sustain cooperative properties such as ferroelectricity, change upon reducing the grain size is critical from both fundamental and applied standpoints. These questions have been addressed in BTO fine-grained ceramics,[12−15] ultrathin films,[16,17] and free-standing nanocrystals.[18−23] Agreement exists on the fact that decreasing the grain size leads to a reduction of coherence length of the ferroelectric coupling between local dipoles and a diminished macroscopic polarization. However, because the phase transitions in this system are size-dependent and become increasingly diffuse in temperature upon reduction of the grain size, controversy remains regarding the possible coexistence of different local symmetries in BTO nanocrystals. Frey and Payne suggested that orthorhombic and tetragonal symmetries coexist in 100 nm grains,[13] whereas Page et al. did not rule out the

Received: April 2, 2012
Published: May 15, 2012

dx.doi.org/10.1021/ja303184w | J. Am. Chem. Soc. 2012, 134, 9475−9487

coexistence of rhombohedral and tetragonal distortions in 5 nm nanocrystals.[23]

In previous studies, the size effect in BTO nanocrystals was investigated employing ensembles of fully grown nanocrystals of varying size.[18−23] Herein, a fundamentally different approach is taken whereby the structural evolution of sub-10 nm BTO nanocrystals formed at room temperature using a vapor diffusion sol−gel method is followed using a series of techniques that probe the atomic structure on different length and time scales. This allows for a comprehensive structural picture of the nanocrystals to be achieved as they nucleate and grow from an amorphous metallorganic gel. Raman spectroscopy and pair distribution function (PDF) analysis of synchrotron X-ray diffraction data show that local dipoles arising from the off-centering of the titanium atom appear to exhibit ferroelectric coupling in the later stages of the nanocrystal growth process. Modeling of the atom−atom pair distribution along with simple geometric analysis of the perovskite structure demonstrate that the local symmetry of these ferroelectric nanoregions, particularly structural correlations within an individual unit cell *and* between two adjacent unit cells, can be best described by the tetragonal space group *P*4*mm*. Furthermore, in contrast with previous PDF studies of sub-10 nm BTO nanocrystals, structural analysis shows that tetragonal *P*4*mm* and orthorhombic *Amm*2 local symmetries may coexist at room temperature. More generally, the comparison between Rietveld and PDF analysis of X-ray diffraction data shows that taking diffuse scattering into account is critical when attempting the structural characterization of nanocrystals.

■ EXPERIMENTAL SECTION

Synthesis of $BaTiO_3$ Nanocrystals. Sub-10 nm BTO nanocrystals were synthesized via a vapor diffusion sol−gel method.[24,25] All manipulations were conducted at room temperature under nitrogen atmosphere using standard Schlenk techniques. All reagents were used as received. A solution of the bimetallic alkoxide $BaTi(OR)_6$ (R = $CH_2CHCH_3OCH_3$) in *n*-butanol/2-methoxypropanol (1:3 v/v) (0.50 M, Gelest, Inc.) was used as the precursor in the synthesis of BTO nanocrystals. The apparatus employed for vapor diffusion has been described in detail elsewhere.[26,27] Briefly, it consists of a 100-mL three-neck reaction flask and a glass bubbler containing a 0.75 M HCl solution; the bubbler, in turn, is connected to the nitrogen manifold via a needle-valve rotameter. In a typical synthesis, 2.0 mL (1.0 mmol) of the bimetallic alkoxide was transferred to the reaction flask. Simultaneously, nitrogen gas was bubbled through the 0.75 M HCl solution for 30 min. Then the bubbler was connected to the reaction flask in order to allow $N_2/HCl/H_2O$ vapor to flow over the precursor solution. An increase in the viscosity of the solution was observed upon continuous flow of vapor. After a certain reaction time, referred to as the gelation time t_g hereafter, this resulted in the formation of a fully rigid and crack-free gel. In this work, the H_2O vapor flow rate was adjusted to obtain $t_g \approx 8$ h and maintained constant throughout the reaction. A few hours after the formation of the monolithic gel, cracks started to appear yielding several small pieces of gel. No precipitation was observed at any point in the process. The vapor flow was stopped after a certain time $t \geq t_g$, referred to as the total reaction time hereafter, and the reaction flask was opened and all the pieces of the gel were collected. These were washed with 5 mL of absolute ethanol, sonicated for 10 min, and centrifuged at 6000 rpm for 25 min; this washing step was repeated three times. The resulting slurry was dried under vacuum at room temperature for 4 h, and the resulting powder was employed in structural and morphological characterization studies thereafter. An identical procedure was followed for each reaction time explored in this work.

Conventional X-ray Diffraction (XRD). Conventional powder XRD patterns were collected in the 20−80° 2θ range using a Rigaku Ultima IV diffractometer operating at 44 mA and 40 kV. Cu Kα radiation (λ = 1.5406 Å) was employed. Diffraction patterns were recorded at 25 °C.

Thermogravimetry (TG). TG analyses were performed using a thermogravimetric analyzer TA Q50 (TA Instruments) under a high-purity nitrogen flow (80 mL min^{-1}). Samples were heated from 30 to 900 °C at a linear rate of 10 °C min^{-1}.

Transmission Electron Microscopy (TEM). TEM images were obtained using a JEOL JEM2100F (JEOL Ltd.) electron microscope operating at 200 kV. Specimens for transmission electron microscopy studies were dispersed in methanol, sonicated for 30 min, and deposited on a 200 mesh Cu grid coated with a Lacey carbon film (Ted Pella, Inc.).

Raman Spectroscopy. Raman spectra were recorded in the 100−1100 cm^{-1} wavenumber range using a Horiba Xplora Raman microscope (Horiba Scientific). Laser radiation of 785 nm wavelength was employed as the excitation source and the power at the sample level was 45 mW. Sulfur and 4-acetamidophenol were employed as frequency standards for calibration of Raman shifts. The absolute accuracy of Raman shifts was estimated to be ±1 cm^{-1}. All spectra were recorded at 25 °C under air.

Synchrotron X-ray Diffraction. Synchrotron XRD patterns for Rietveld analysis[28,29] were collected in the 5−40° 2θ range at the 11−BM line of the Advanced Photon Source of Argonne National Laboratory. An incident photon energy of 30.013 keV (λ = 0.413106 Å) was employed. Diffraction patterns were collected in transmission mode at 25 °C. Rietveld structural refinements were carried out using the General Structure Analysis System (GSAS) software.[30] Experimental data and atomic X-ray scattering factors were corrected for sample absorption and anomalous scattering, respectively. The following parameters were refined: (1) scale factor, (2) background, which was modeled using a shifted Chebyschev polynomial function, (3) peak shape, which was modeled using a modified Thomson−Cox−Hasting pseudovoight function including an asymmetry parameter,[31] (4) lattice constants, (5) fractional atomic coordinates of the titanium atom(s) when allowed by symmetry, and (6) an isotropic thermal parameter for each chemical species, regardless of their crystallographic site in the perovskite structure (i.e., U_{Ba}, U_{Ti}, and U_O). The usual R_{wp} and χ^2 indicators were employed to assess the quality of the refined structural models.[32]

Synchrotron XRD patterns for PDF analysis were collected at the 11−ID−B line of the Advanced Photon Source of Argonne National Laboratory. An incident photon energy of 90.484 keV (λ = 0.137024 Å) was employed. Diffraction data were collected in transmission mode at 25 °C. In this work, the pair distribution function $G(r) = 4\pi r[\rho(r) - \rho_0]$ was employed for structural analysis, where r is the radial distance, and $\rho(r)$ and $\rho_0(r)$ are the local and average atomic number density, respectively. The RAD software was employed to extract $G(r)$ from the raw diffraction data.[33] To this end, these data were first corrected for background, sample absorption, and Compton scattering. Then, properly normalized structure functions $S(Q)$ were obtained; these are given in the Supporting Information as $Q[S(Q) - 1]$, where Q is the scattering vector. Finally, $S(Q)$ was Fourier-transformed using a maximum momentum transfer (Q_{max}) of 25 Å^{-1} to yield $G(r)$. PDF structural refinements were carried out using the PDFgui software.[34] The following parameters were refined: (1) scale factor, (2) lattice constants, (3) fractional atomic coordinates of the titanium atom when allowed by symmetry, and (4) an isotropic thermal parameter for each chemical species, regardless of their crystallographic site in the perovskite structure. The R_{wp} indicator was employed to assess the quality of the refined structural models.[35]

■ RESULTS AND DISCUSSION

1. Conventional X-ray Diffraction. The formation of BTO nanocrystals from the bimetallic $BaTi(OCH_2CHCH_3OCH_3)_6$ alkoxide upon continuous flow of H_2O vapor proceeds via hydrolysis and polycondensation. The formation of BTO nanocrystals was monitored by conventional XRD and diffraction patterns corresponding to fresh samples collected after a total reaction time $t \geq t_g$ are shown in Figure 1.

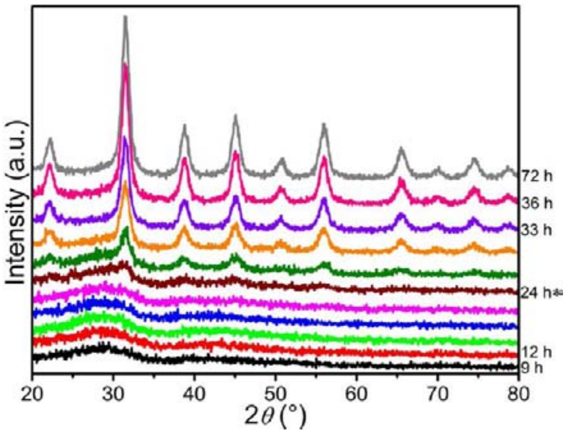

Figure 1. XRD patterns of BTO samples prepared via vapor diffusion sol−gel with a gelation time of ~8 h; the total reaction time for each sample is indicated in the right axis. Collection of samples began 1 h after gelation and, unless indicated, continued in 3 h increments thereafter. The reaction time corresponding to the onset of crystallinity is denoted with the * symbol.

Diffraction maxima develop upon continuous flow of H_2O vapor, indicating the gel resulting from the hydrolysis and condensation of the bimetallic alkoxide precursor undergoes an amorphous-to-crystalline phase transition. The onset of crystallinity appears after 24 h and no further changes in the intensity of the diffraction maxima are observed after 36 h, indicating the phase transition is complete at that point. Fresh BTO nanocrystals appear phase pure, with no observable traces of $BaCO_3$, TiO_2, or pyrochlore-type phases. All the diffraction maxima can be indexed to the cubic perovskite phase with space group $Pm\bar{3}m$ (ICSD No. 67518) and lattice constant $a \approx$ 4.01 Å.

2. Thermogravimetry. The formation of BTO nanocrystals from the amorphous gel was also followed via TG analysis. Thermograms corresponding to samples collected after a total reaction time of 8, 15, 24, 30, 36, and 72 h are given in the Supporting Information; these exhibit a total weight loss of ~22, 19, 16, 13, 11, and 9 wt %, respectively. For all samples, the main weight losses occur below 600 °C and arise from the desorption of H_2O and decomposition of the remaining organic matrix. The more extended hydrolysis and polycondensation of the bimetallic alkoxide precursor at longer reaction times leads to an increase in the amount of alkoxy ligands expelled from the gel as alcohol. This, in turn, leads to a decrease of the organic content in the gel, which translates into the observed decrease in the total weight loss upon increasing the total reaction time.

3. Transmission Electron Microscopy. The morphological evolution of the amorphous gel into BTO nanocrystals was monitored via TEM. Images corresponding to samples collected after a total reaction time of 12, 27, 30, and 72 h are shown in Figure 2a−d; images for samples collected at other reaction times are given in the Supporting Information. The evolution of the estimated particle size distribution with the total reaction time is given in Figure 2e. Two groups of samples can be distinguished on the basis of their morphological features. The first group consists of samples collected after a total reaction time ranging from 12 to 27 h. Submicrometer-sized amorphous pieces of the gel are observed in these samples with no discrete nanocrystals present. However, observation of well-defined lattice fringes under high-resolution and variable focus reveals the presence of crystalline areas embedded within the amorphous material; the spacing of the lattice fringes equals 0.29 nm, corresponding to the {110} crystal planes of the perovskite phase. Typically, these crystalline areas exhibit a diameter ranging from 3 to 6 nm and their volume fraction within the amorphous matrix increases upon increasing the total reaction time, in agreement with XRD data.

The second group includes samples collected after a total reaction time ranging from 30 to 72 h. In this group, well-defined and dispersed BTO nanocrystals are clearly noticeable; only the sample collected at 30 h exhibits signs of agglomeration. For this sample, a minor fraction of BTO nanocrystals appears embedded within fiber-like pieces of an amorphous gel network, indicating the amorphous-to-crystalline phase transition is not complete at this point. Nanocrystals exhibit a mean diameter of ~9 nm, which appears to remain constant upon increasing the total reaction time from 30 to 72 h. Although the average grain diameter for these samples appears constant by TEM, the contraction of the perovskite unit cell as the total reaction time increases reveals an increase in the size of the crystalline domains, indicating the crystallization of amorphous material located in outer region of the grains takes place (*vide infra*). High-resolution TEM imaging of individual nanocrystals shows the presence of well-defined lattice fringes corresponding to the {110} crystal planes of the perovskite phase, suggesting that these particles are single crystalline. The spacing of the fringes changes from 0.29 to 0.28 nm upon increasing the reaction time from 30 to 72 h, demonstrating that a slight contraction of the unit cell is taking place.

4. Raman Spectroscopy. Owing to the shorter coherence length and time scale of the physical phenomenon it probes, Raman spectroscopy is particularly sensitive to local structural distortions that are space- and time-averaged by XRD. Raman spectra of samples collected after a total reaction time of 24, 27, 30, 33, 36, and 72 h are shown in Figure 3. The spectrum of the sample collected at 24 h is featureless, demonstrating the predominantly amorphous character of the gel. Increasing the reaction time to 27 h leads to the appearance of weak and broad Raman bands at 177, 272, 534, 677, 740, and 816 cm^{-1}, indicating the development of areas with increased structural coherence relative to earlier reaction times. Most of these vibrational bands significantly increase in intensity and decrease in width upon increasing the reaction time to 30 h, demonstrating the increased structural coherence. This observation is in good agreement with XRD and TEM data for this group of samples, which showed that at 27 h a major fraction of the gel is amorphous and only a very minor fraction is crystalline, whereas the situation is the opposite at 30 h. Raman spectra of samples collected at 30 and 33 h are identical and consist of broad bands at 177, 272, 521, 685, 740, and 807 cm^{-1}. Increasing the reaction time to 36 h results in the following changes: (1) an increase in band intensity and a decrease in bandwidth; (2) the two bands at 685 and 740 cm^{-1} merge into a single band at ~700 cm^{-1}; and (3) the appearance of sharp peaks at 136, 225, 153, 689, and 1058 cm^{-1}. The spectra of samples collected at 36 and 72 h also appear nearly identical to each other.

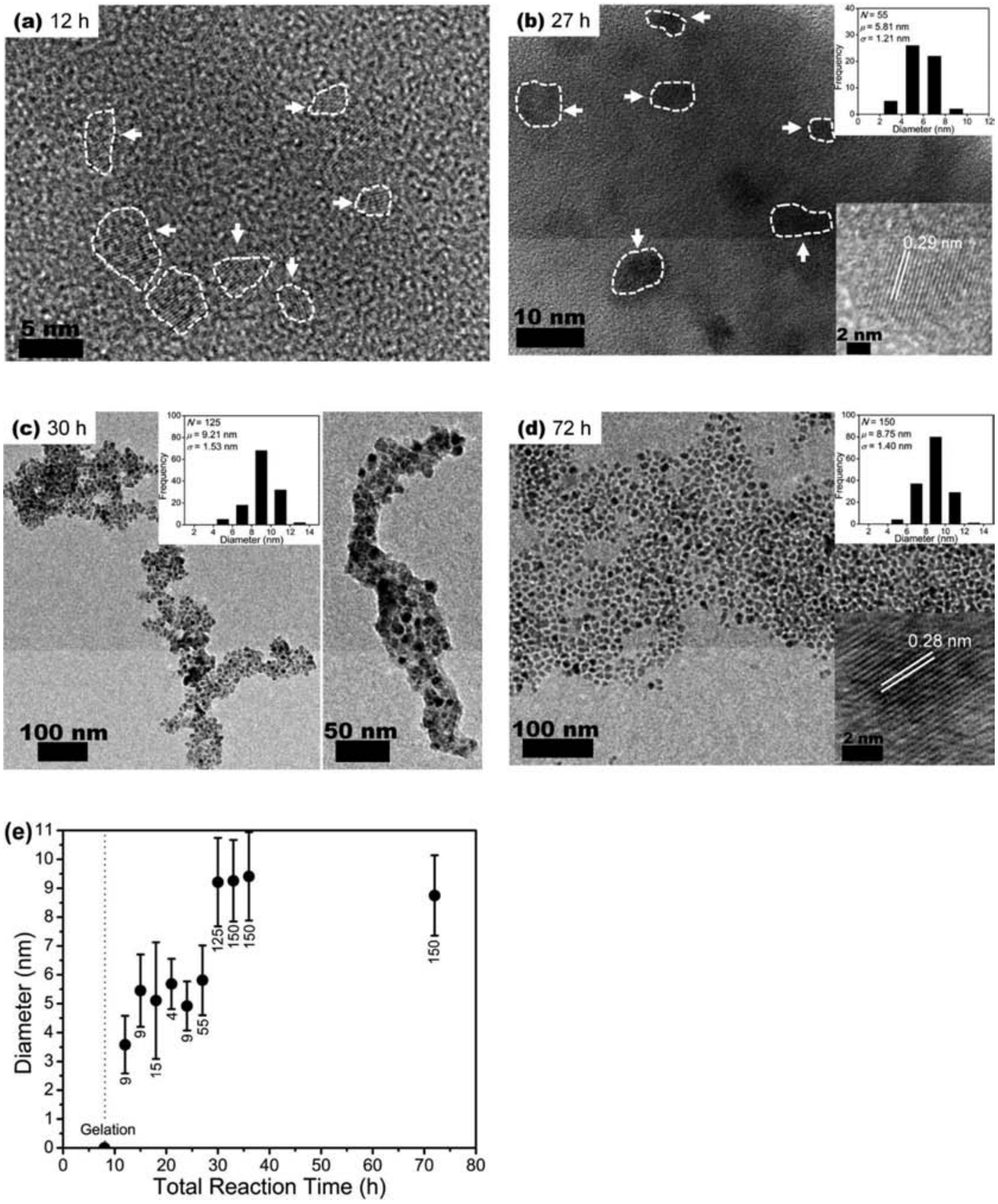

Figure 2. TEM images of BTO samples collected at: (a) 12, (b) 27, (c) 30, and (d) 72 h. Crystalline areas in (a) and (b) are denoted with white arrows and dotted lines. Nanocrystals embedded in fiber-like pieces of the amorphous gel observed in (c) are shown in the right panel. Particle size distribution histograms and high-resolution images showing lattice fringes corresponding to the {110} crystal planes are given in the insets. (e) Particle size distribution as a function of the total reaction time; the total number of particles counted is given (see text for details).

Assignment of the vibrational bands described above to specific vibrational modes of BTO can be carried out on the basis of previous Raman investigations of single crystal,[5,36−38] bulk,[21,39,40] thin-film,[41] and nanocrystalline BTO.[21] To this end, the spectrum of the sample collected at 72 h will be employed; this spectrum shows more intense and narrow bands which facilitate their assignment. Samples employed in Raman spectroscopic studies were previously exposed to air in order to carry out XRD analysis. Peaks at 136, 153, 225, 689, and 1058 cm^{-1} denote the presence of $BaCO_3$ arising from the reactive adsorption of atmospheric CO_2 on the highly basic BaO surface layers of the BTO nanocrystals.[40,42,43] Bands at 177, 272, 521, and ~700 cm^{-1} arise from crystalline BTO. Tentative assignments are given in Figure 3. Bands at 272 and 521 cm^{-1} have been observed in both the cubic and tetragonal phase of BTO and were conclusively assigned to scattering from A_1(TO) phonons.[5,13,19,21,22,36,38,40,41] Because first-order Raman scattering is symmetry-forbidden in the centrosymmetric $Pm\bar{3}m$ space group, the activation of these phonons has been attributed to the presence of non-centrosymmetric regions in which the titanium atom is displaced from the center of the TiO_6 octahedra.[38] The band at ~700 cm^{-1} has been observed in the tetragonal phase of BTO and assigned to the A_1(LO) and E(LO) phonons.[21,38−41,44] This band and a sharp peak at ~305 cm^{-1} are considered to be the Raman signature of the tetragonal phase. This prompted us to

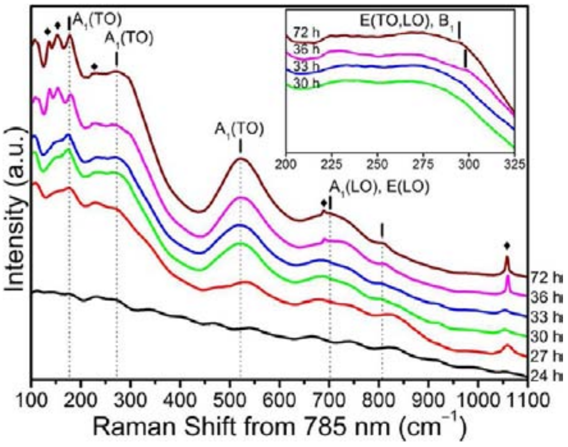

Figure 3. Raman spectra of selected BTO samples; the total reaction time for each sample is indicated in the right axis. Bands arising from the perovskite phase are denoted with the | symbol, and their assignment to specific phonons is given. Bands arising from surface $BaCO_3$ are denoted with the ◆ symbol. Inset: expanded spectra of samples collected at 30, 33, 36, and 72 h.

investigate the possibility that non-centrosymmetric tetragonal regions develop as BTO nanocrystals grow from the amorphous gel. Thus, careful attention was paid to the presence of a peak at ~305 cm^{-1}; expanded spectra for samples collected at 30, 33, 36, and 72 h are shown in the 200–325 cm^{-1} wavenumber range in the inset of Figure 3. Very weak shoulders at 299 and 296 cm^{-1} are observed in the spectra of samples collected at 36 and 72 h, respectively. These shoulders are assigned to the E(TO), E(LO), and B_1 phonons of non-centrosymmetric tetragonal BTO. The sharp peak at 177 cm^{-1} arises from the coupling of A_1(TO) phonons.[21,38,44] Finally, no assignment of the shoulder at ~807 cm^{-1} can be made at present. Although Shiratori and co-workers observed a similar feature in nanocrystalline BTO and assigned it to a lattice defect vibrational mode,[21] a conclusive assignment has not been reported yet.

The weak intensity of the vibrational bands of BTO nanocrystals, as well as their broadness, is typical of heavily damped phonons. Likewise, the presence of a peak at ~177 cm^{-1} rather than the dip observed in polycrystalline BTO with average grain diameter larger than 100 nm[21,44] indicates a weak coupling between the A_1(TO) phonons. Both observations confirm the reduced structural coherence of nanocrystals with respect to their single crystal and bulk counterparts. The presence of non-centrosymmetric regions that result from the local off-centering of the titanium atoms is also confirmed. Most important in the perspective of this work is the observation that the coherence of the local displacements of the titanium atom increases with increasing reaction time, ultimately leading to the development of non-centrosymmetric tetragonal (i.e., ferroelectric) regions after 36 h. This finding was further confirmed by synchrotron XRD (*vide infra*). This can be rationalized by considering that atomic positional disorder in general, and of titanium in particular, decreases as the amorphous-to-crystalline phase transition progresses. This results in an increase in the spatial range to which local tetragonal distortions can propagate coherently or, equivalently, an increase in the mean free path of the phonons associated with those distortions.

5. Synchrotron X-ray Diffraction. *Rietveld Analysis.* Synchrotron XRD was performed in order to gain quantitative insight into the structural evolution of BTO nanocrystals as they grow from the amorphous metallorganic gel. Rietveld analysis of the experimental diffraction patterns was carried out using the centrosymmetric, cubic $Pm\overline{3}m$ space group. A $BaCO_3$ phase (ICSD No. 158378, orthorhombic space group *Pmcn*)[45] was included when needed; for this phase, the scale factor, peak shape, and lattice constants were refined. Synchrotron XRD patterns and Rietveld fits for samples collected at 27 and 30 h are shown in Figure 4a,b; experimental and calculated patterns

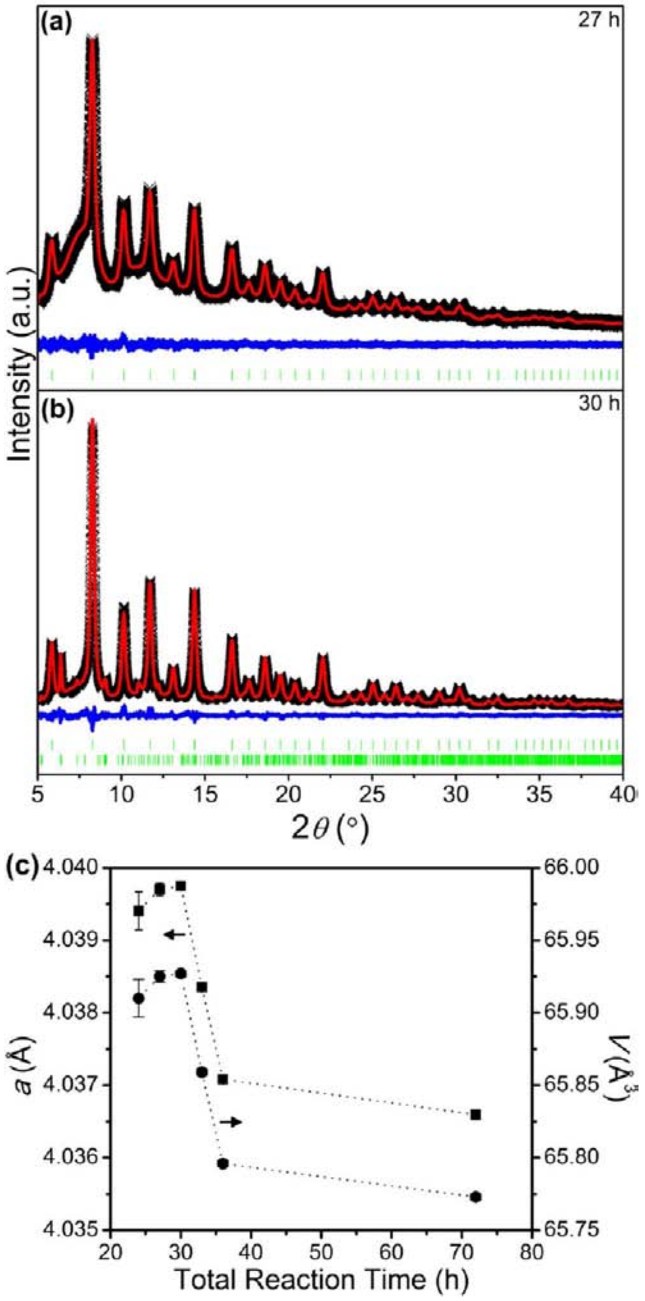

Figure 4. Rietveld analysis of synchrotron XRD patterns of BTO samples collected at (a) 27 and (b) 30 h. Experimental (×) and calculated (red line) patterns are shown for each sample along with the difference curve (blue line) and ticmarks (|) corresponding to the phase(s) refined. For the 30 h sample, upper and lower tickmarks correspond to cubic $BaTiO_3$ and orthorhombic $BaCO_3$, respectively. (c) Evolution of the lattice constant *a* and unit cell volume *V* with the total reaction time. Dotted lines are guides to the eye.

Table 1. Rietveld Analysis of Synchrotron X-ray Diffraction Data of $BaTiO_3$ Nanocrystals

Space Group $Pm\bar{3}m$

t (h)	a (Å)	V (Å^3)	U_{Ba} (Å^2)[a]	U_{Ti} (Å^2)[a]	U_O (Å^2)[a]	$BaCO_3$ (wt %)[b]	R_{wp}	χ^2
24	4.0394(3)	65.910(13)	1.39(10)	2.82(12)	0.96(14)	–	3.11	0.77
27	4.0397(1)	65.925(4)	0.89(3)	2.05(4)	0.34(5)	–	2.85	0.84
30	4.03974(5)	65.927(2)	0.868(14)	1.799(17)	0.24(3)	6.64(3)	3.98	1.62
33	4.03835(4)	65.859(2)	0.910(13)	1.659(16)	0.14(2)	6.33(3)	4.33	1.91
36	4.03708(4)	65.796(2)	0.930(13)	1.495(15)	0.1(2)	11.40(3)	4.65	2.15
72	4.03659(5)	65.773(2)	1.018(17)	1.38(2)	−0.1(3)	16.08(4)	5.13	2.50

Space Group $P4mm$

t (h)	a, c (Å)	V (Å^3)	z_{Ti}	U_{Ba} (Å^2)[a]	U_{Ti} (Å^2)[a]	U_O (Å^2)[a]	$BaCO_3$ (wt %)[c]	R_{wp}	χ^2
36	4.03208(12), 4.0482(3)	65.814(2)	0.4427(4)	1.282(16)	−0.75(3)	−0.27(2)	11.33(3)	4.37	1.90
72	4.03102(13), 4.0493(3)	65.797(2)	0.4411(3)	1.48(2)	−1.03(3)	−0.48(3)	15.90(4)	4.82	2.21

[a] Given as 100 × U. [b] Lattice parameters (a, b, c): (a) 30 h: 5.2779(6), 8.9725(12), 6.4394(8) Å; (b) 33 h: 5.2754(6), 8.9781(11), 6.4427(8) Å; (c) 36 h: 5.2721(3), 8.9767(6), 6.4237(4) Å; and (d) 72 h: 5.2721(3), 8.9751(6), 6.4289(4) Å. [c] Lattice parameters (a, b, c): (a) 36 h: 5.2722(3), 8.9764(6), 6.4240(4) Å; and (b) 72 h: 5.2721(3), 8.9747(5), 6.4291(4) Å.

of samples collected at 21, 24, 33, 36, and 72 h are given in the Supporting Information. Structural parameters extracted from Rietveld analysis are plotted in Figure 4c and summarized in Table 1.

Two groups of samples could be distinguished upon visual inspection of the experimental diffraction patterns. The first group includes samples collected after a total reaction time ranging from 24 to 27 h. The diffraction pattern of the sample collected at 27 h (Figure 4a), which is representative of this group, exhibits significant diffuse scattering in addition to coherent (i.e., Bragg) scattering. The second group includes samples collected after a total reaction time ranging from 30 to 72 h, and, like in the pattern of the sample collected at 30 h (Figure 4b), diffraction data are dominated by coherent scattering. These observations are in good agreement with TEM data that showed that samples belonging to the first group consist of a major amorphous volume fraction, while samples belonging to the second group consist of discrete ~9 nm diameter nanocrystals. The attenuation of diffuse scattering as the amorphous-to-crystalline phase transition progresses is reflecting an increase in structural coherence through a decrease in atomic positional disorder.

Rietveld analysis of the experimental patterns of the first group of samples shows that all the diffraction maxima can be indexed to the perovskite phase, with no secondary crystalline phases observable. In our attempts to fit the proposed structural model to the experimental data, a high correlation between the lattice constant a and the number of parameters employed to model the background was observed. Indeed, although the background could be adequately modeled, this was achieved at the expense of introducing a large number of parameters in the polynomial expansion; this, in turn, invariably resulted in χ^2 values lower than unity (i.e., overparametrization of the model). As a consequence, the estimated standard deviations of the lattice constant were abnormally high (see Table 1). Therefore, the reliability of the structural parameters derived for this group of samples is compromised by the inability of Rietveld analysis to handle materials exhibiting large atomic positional disorder, which results in significant diffuse scattering in their diffraction patterns.

Rietveld analysis of the experimental diffraction patterns of the second group of samples shows that diffraction maxima in these patterns can be indexed to the perovskite $BaTiO_3$ and to orthorhombic $BaCO_3$. Inspection of the evolution of the refined structural parameters upon increasing the reaction time reveals a contraction of the perovskite unit cell as the total reaction time increases (Figure 4c). This observation can be rationalized by considering that the size of the crystalline domains within individual grains increases as amorphous material is consumed. This finding has been extensively reported for oxides in general,[46−48] and for BTO in particular.[22,44,47−50] It should be noted that the magnitude of the contraction of the unit cell is significantly larger on going from 30 to 36 h than from 36 to 72 h, indicating that the consumption of amorphous material is nearly completed at 36 h and that only marginal growth occurs thereafter. Likewise, the increase in the weight fraction of surface carbonate with reaction time, according to 72 > 36 > 33 ≈ 30 h, reflects an enhanced crystallinity of the perovskite grains, since chemisorption of atmospheric CO_2 requires the presence of BTO nanocrystals with well-crystallized BaO surface layers exposed.

Because Raman spectroscopy indicated the likely presence of polar tetragonal distortions in samples collected at 36 and 72 h, modeling of their experimental diffraction patterns with the non-centrosymmetric, tetragonal $P4mm$ space group was attempted. The fractional atomic coordinate z of the titanium atom (z_{Ti}) was refined, while oxygen atoms were held fixed at ($^1/_2$,0,$^1/_2$) and ($^1/_2$,$^1/_2$,0). The resulting structural parameters have been included in Table 1; graphical fits are given in the Supporting Information. Judging by the values of the goodness-of-fit R_{wp}, the tetragonal space group provides a slightly better description of the crystal structure than the cubic one. However, inspection of the calculated values of thermal parameter U_{Ti} shows the former yields physically unrealistic values, whereas the latter does not. Therefore, the slightly smaller value of R_{wp} for the tetragonal model can be attributed to an increased number of internal degrees of freedom rather than to a more accurate description of the actual crystal structure. Visually, the fits were identical and both models appeared indistinguishable to synchrotron XRD.

It is worth noting at this point that U_O values calculated using a cubic model are abnormally low (i.e., $U_O < U_{Ti}$ and $U_O < 0$) for samples collected at 30 h and after. These results demonstrate that, although much weaker than coherent scattering,[51] diffuse scattering contributes to the diffraction patterns of this group of nanocrystals. As shown below, this

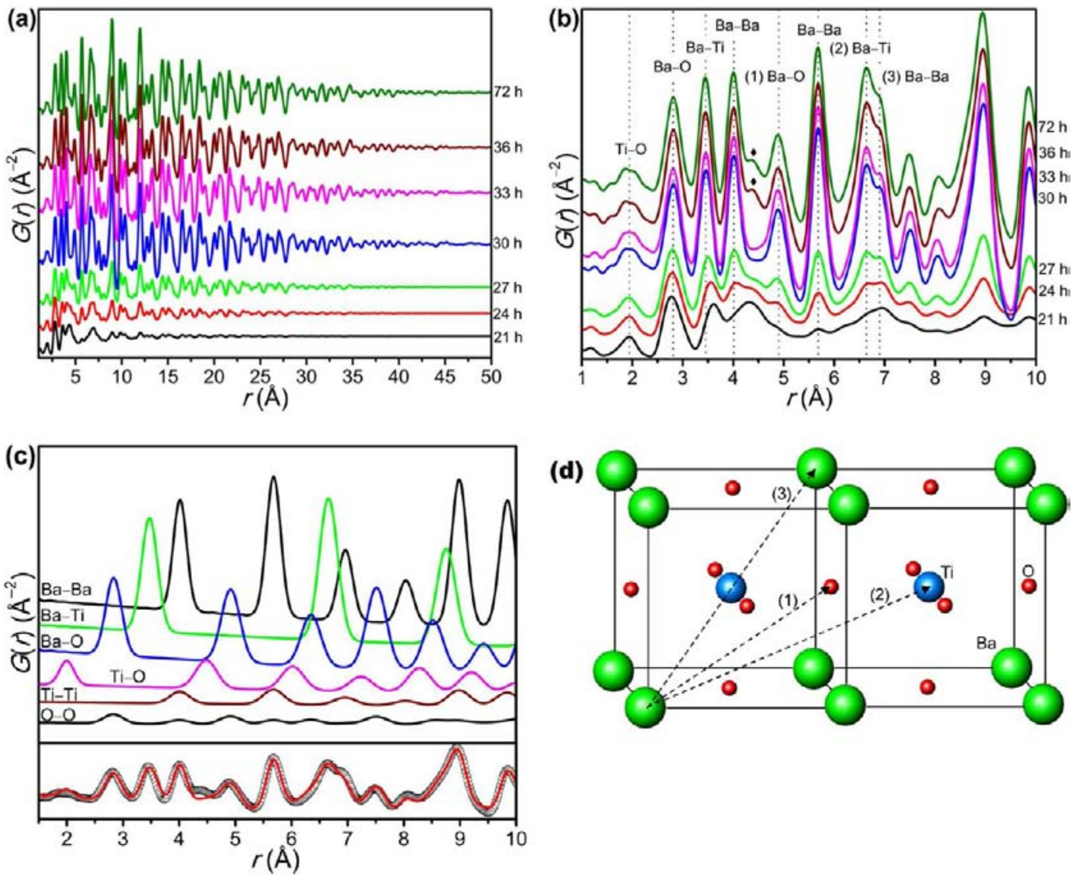

Figure 5. Experimental PDFs of selected BTO samples displayed in the: (a) 1−50, and (b) 1−10 Å distance range; the total reaction time for each sample is indicated in the right axis. Atom−atom pairs contributing to the peaks between 1.5 and 7 Å are given in (b); the peak located at ∼4.4 Å and denoted with the ◆ symbol arises from Ba−Ba pairs in $BaCO_3$. (c) Decomposition of the total PDF calculated using the $Pm\bar{3}m$ space group into partial atom−atom pair contributions; the contribution of atoms from the $BaCO_3$ phase is not included. The bottom panel shows the experimental PDF (○) and the sum of partial PDFs (red line). (d) Geometric analysis of the perovskite unit cell depicting atom−atom pairs: (1) Ba−O (4.9 Å), (2) Ba−Ti (6.6 Å), and (3) Ba−Ba (6.9 Å). PDFs in each panel are displayed in the same scale, offset for clarity.

contribution must be taken into account if an adequate structural picture is to be achieved.

Pair Distribution Function Analysis. Unlike Rietveld analysis, PDF is a total scattering technique that allows both the coherent and diffuse components of the XRD pattern to be properly accounted for when modeling a crystal structure. A particular strength of this technique is the potential to interrogate the material's structure within variable spatial ranges. Specifically in the case of nanocrystals exhibiting local structural distortions, this allows the study of the evolution of the local crystal structure into the average structure as well as extraction of the correlation length of the distortions.

In this work, PDF analysis of the diffraction data was employed to study the structural evolution of BTO nanocrystals with respect to total reaction time and atom−atom pair distance. Synchrotron X-ray PDFs were obtained for samples collected after a total reaction time of 21, 24, 27, 30, 33, 36, and 72 h; these are shown in the 1−50 Å distance range in Figure 5a. Two groups of samples can be distinguished upon visual inspection of the experimental PDFs. The first group consists of samples collected after a total reaction time ranging from 21 to 27 h, while the second includes samples collected at 30 h and after. PDFs of samples belonging to the first group exhibit weak and broad peaks, whereas those of the second group show intense and narrow peaks. The intensity and width of the peaks increases and decreases, respectively, with increasing reaction time; an increase in the range to which peaks expand is also observed. These changes are particularly obvious upon increasing the reaction time from 21 to 30 h and reflect an increase in structural coherence, i.e., a decrease in atomic disorder as a result of the formation of Ba and Ti coordination polyhedra and their subsequent assembly into a periodic structure. This is in good agreement with XRD, TEM, and Raman data. Interestingly, PDFs for samples collected at 21, 24, and 27 h exhibit peaks that vanish at 20, 30, and 35 Å, respectively. These distances are much shorter than the average diameter of the crystalline areas observed by TEM, which was in the range of ∼50−60 Å (5−6 nm) for these samples. Likewise, samples collected after a total reaction time ranging from 30 to 72 h appear as ∼90 Å (9 nm) nanocrystals by TEM, but their PDFs become featureless after 45 Å. A similar finding was reported by Petkov et al., who found that the PDF of 5 nm BTO nanocrystals vanished after 2 nm.[15,20] Similarly, Gilbert et al. observed that the PDF of 3.4 nm diameter ZnS nanocrystals vanished after 2.0 nm.[52] As stated by Petkov and co-workers, these findings demonstrate that nanocrystals not only lack the usual extended periodicity observed in bulk form, but they also exhibit significant atomic positional disorder that leads to a further reduction of their structural coherence. Gilbert et al. showed that inhomogeneous internal strain contributes to this loss of structural coherence as well.

Expanded experimental PDFs are shown in the 1−10 Å distance range in Figure 5b. The atom pair distribution of samples collected at 30, 33, 36, and 72 h are very similar to each other and can be, in principle, well matched to that of a unit cell with $Pm\bar{3}m$ space group and lattice constant a = 4.02 Å. Decomposition of the total PDF calculated using such a structure into partial atom−atom pair PDFs (Figure 5c) and geometric analysis (Figure 5d) show that peaks at ~2.0, 2.8, 3.5, 4.0, 4.9, and 5.7 Å correspond to atomic pairs Ti−O ($d = a/2$), Ba−O ($d = a\sqrt{2}/2$), Ba−Ti ($d = a\sqrt{3}/2$), Ba−Ba (edge, $d = a$), Ba−O (nonadjacent atoms, $d = (a^2 + (a/2)^2 + (a/2)^2)^{1/2}$), and Ba−Ba (face diagonal, $d = a\sqrt{2}$), respectively. Important in the context of this work is the doublet consisting of a peak located at ~6.6 Å and a shoulder at ~6.9 Å. The latter was assigned by Petkov and co-workers to correlations between oxygen atoms from neighboring TiO_6 octahedra; however, no detailed structural basis was provided for that assignment.[20] Geometric analysis shows this shoulder can be well matched to a Ba−Ba pair located along the unit cell diagonal ($d = a\sqrt{3}$) and that no correlations between adjacent unit cells must be invoked. Instead, it is the peak at ~6.6 Å that describes interactions between neighboring unit cells. As shown in Figure 5d, this peak arises from Ba−Ti pairs located in adjacent unit cells ($d = ((a/2)^2 + (3a/2)^2 + (a/2)^2)^{1/2}$). Finally, it should be noted that PDFs corresponding to the samples collected at 36 and 72 h also show a weak peak at ~4.4 Å arising from the presence of substantial amounts of surface $BaCO_3$; indeed, this phase features Ba−Ba distances of ~4.3 and 4.5 Å.

Quantitative insight into the structural evolution of BTO nanocrystals with respect to total reaction time and atom−atom distance was gained by fitting different structural models to the experimental data; a two-step modeling strategy was employed to this end. First, fits of the cubic $Pm\bar{3}m$, tetragonal $P4mm$, orthorhombic $Amm2$, and rhombohedral $R3m$ space groups to the experimental PDF of the sample collected at 72 h were attempted in the 1.5−20 Å distance range. The starting crystal structures were taken from the work of Kwei et al.[1,53] The crystal structure of the $BaCO_3$ phase was that given by Rietveld analysis of the corresponding diffraction pattern; a scale factor was refined for this phase. The experimental and calculated PDFs are shown in Figure 6, and the calculated structural parameters are summarized in Table 2. Inspection of these results shows that in the 1.5−20 Å distance range:

- PDF analysis of the XRD data does not yield unphysical values for any of the refined structural parameters, in contrast to Rietveld analysis.
- Non-centrosymmetric space groups $P4mm$, $Amm2$, and $R3m$ give a better fit to the experimental data than centrosymmetric $Pm\bar{3}m$, according to $R_{wp}^{P4mm} \approx R_{wp}^{Amm2} < R_{wp}^{R3m} \ll R_{wp}^{Pm\bar{3}m}$.
- Tetragonal and orthorhombic symmetries provide a better fit than rhombohedral symmetry, with the tetragonal space group $P4mm$ providing the best fit. In particular, the space group $P4mm$ provides a better fit than the $Amm2$ space group despite having a smaller number of internal degrees of freedom.

These findings demonstrate that accounting for diffuse scattering is critical when attempting the structural characterization of nanocrystals with XRD. Indeed, PDF analysis of synchrotron XRD data allows non-centrosymmetric and centrosymmetric space groups to be clearly distinguished. Therefore, it provides a significantly more reliable structural picture than Rietveld analysis.

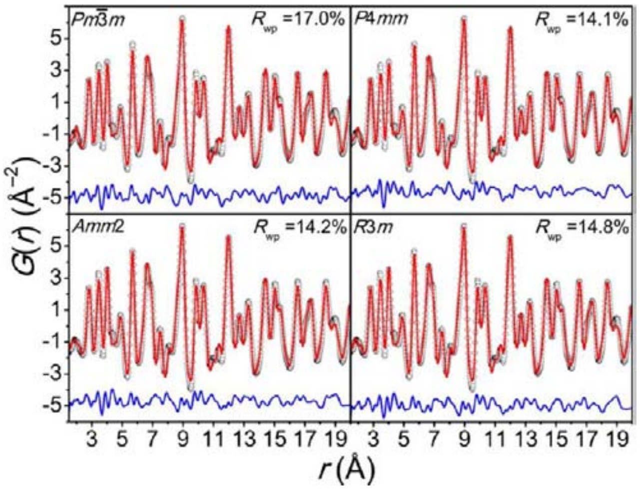

Figure 6. PDF analysis of synchrotron XRD data of BTO nanocrystals collected at 72 h. Fits in the 1.5−20 Å distance range are shown for space groups $Pm\bar{3}m$, $P4mm$, $Amm2$, and $R3m$. The experimental (○) and calculated (red line) PDF are shown along with the difference curve (blue line); the latter has been offset for clarity.

Most important, results outlined above have implications for the description of the room-temperature crystal structure of sub-10 nm BTO nanocrystals. First, they confirm the presence of non-centrosymmetric regions in this sample, in agreement with Raman data. Second, they provide fundamental insight into the local structure of these polar regions. In order to understand the ability of the tetragonal $P4mm$ space group to provide a better fit to the experimental data, we carefully compared the graphical fits obtained for all of the space groups attempted. Two notable differences were observed and are shown in Figure 7a: (1) neither the cubic nor the rhombohedral model accurately reproduces the peaks at ~6.6 and 6.9 Å, whereas both the tetragonal and the orthorhombic models do, and (2) the cubic and the rhombohedral models lead to a pronounced shoulder at ~17.1 Å, which is not observed in the experimental data. We now turn our attention to the first of these features, that is, the peak located at ~6.6 Å and the shoulder at ~6.9 Å. It is observed that PDFs calculated using tetragonal and orthorhombic models feature a local maximum at 6.64 Å, which is in good agreement with the experimental data. In contrast, the cubic and rhombohedral models exhibit a local maximum at 6.66 and 6.68 Å, respectively. The disagreement with the experimental data is particularly obvious in the case of the cubic model. Decomposition of the total PDF into the partial PDFs of atom−atom pairs contributing to the doublet (i.e., Ba−Ti and Ba−Ba) shows that cubic and rhombohedral space groups yield the first component of the doublet at higher r values than tetragonal and orthorhombic models (Figure 7b); however, all four space groups lead to a second component at the same r value (i.e., 6.96 Å). The full width at half-maximum of the peak arising from the Ba−Ti pair was found to be 0.383, 0.373, 0.375, and 0.38 Å for space groups $Pm\bar{3}m$, $P4mm$, $Amm2$, and $R3m$, respectively. For the peak corresponding to the Ba−Ba pair, values of 0.308, 0.297, 0.301, and 0.310 Å were obtained, respectively. The ratio of the integrated intensity of the first component to that of the second component of the doublet was found to be 2.50 for all space groups. Therefore, the

Table 2. PDF Analysis of Synchrotron X-ray Diffraction Data of $BaTiO_3$ Nanocrystals Collected After 72 h

space group[a]	lattice parameter(s)	Ti (x,y,z)	U_{Ba} (Å^2)[b]	U_{Ti} (Å^2)[b]	U_O (Å^2)[b]	$BaCO_3$ (wt %)[c]	R_{wp}
$Pm\bar{3}m$	a = 4.0216(8) Å	0, 0, 0	1.14(6)	2.47(17)	2.9(3)	17(2)	17.0
$P4mm$	a = 4.004(3) Å c = 4.056(7) Å	$^1/_2$,$^1/_2$,0.468(6)	0.96(10)	1.4(3)	2.7(3)	16(2)	14.1
$Amm2$	a = 3.994(8) Å b = 5.675(12) Å c = 5.740(11) Å	$^1/_2$,0,0.524(5)	0.95(13)	1.2(3)	2.4(3)	17(2)	14.2
$R3m$	a = 4.0215(11) Å α = 89.59(12)°	0.481(4), 0.481(4), 0.481(4)	1.03(11)	1.3(4)	2.4(3)	17(2)	14.8

[a] Input crystal structures taken from ref 1.[53] [b] Given as 100 × U. [c] Crystal structure given by Rietveld analysis.

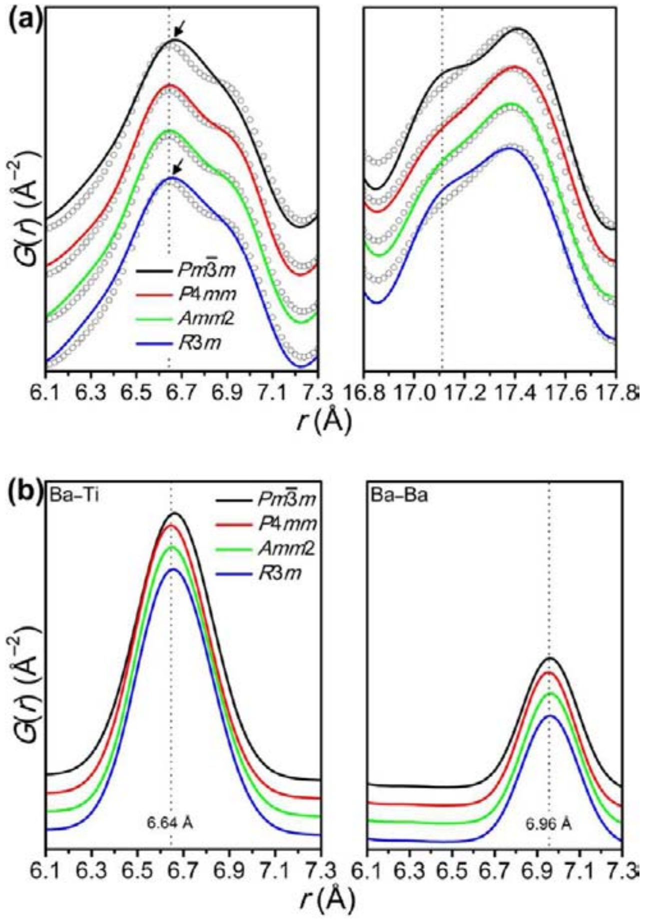

Figure 7. (a) Expanded fits of $Pm\bar{3}m$, $P4mm$, $Amm2$, and $R3m$ space groups to the experimental PDF (○) of BTO nanocrystals collected at 72 h. Arrows depict the misfit of the cubic and rhombohedral models to the peak at 6.64 Å. (b) Contributions of the Ba−Ti (left panel) and Ba−Ba (right panel) atom pairs to the peaks at 6.64 and 6.96 Å. The experimental and calculated partial atom−atom PDFs are shown in the same scale, offset for clarity.

inability of the cubic and rhombohedral models to adequately reproduce the observed doublet is caused by the misfit of the peak at ~6.6 Å which appears shifted to higher r values, thereby leading to a less pronounced shoulder at ~6.9 Å. Conversely, tetragonal and orthorhombic models yield the first component in the correct position with slightly narrower peaks, resulting in a better resolved doublet. Recalling that the peak width depends on structural (i.e., static) and vibrational (i.e., thermal) disorder, and that the peak at 6.64 Å arises from Ba−Ti located in adjacent unit cells, it can be concluded that the tetragonal $P4mm$ space group gives a more accurate description of structural correlations within an individual unit cell *and* between two adjacent unit cells. From this perspective, it is not surprising that an acentric orthorhombic symmetry group in which $b \approx c$ is also able to adequately describe the local crystal structure.

The main implication of this result is that, although the presence of acentric regions with tetragonal symmetry can be unambiguously stated, the existence of regions with orthorhombic symmetry cannot be ruled out, in striking contrast with previous PDF studies of BTO nanocrystals with average diameters ranging from 5 to 100 nm. Indeed, Page et al.[23] suggested that regions with rhombohedral rather than orthorhombic symmetry could be present in ~5 nm diameter nanocrystals in addition to those with tetragonal symmetry. Studying nanocrystals of similar size, Petkov et al. ruled out the possible presence of regions with rhombohedral and orthorhombic symmetry based on the much higher values of R_{wp} (R_{wp}^{P4mm} = 21% ≪ R_{wp}^{Amm2} = R_{wp}^{R3m} = 27%),[20] a trend these authors attributed to the broader distribution of Ti−O distances that resulted in a misfit of the experimental peak at ~2.0 Å. In this work, a definite misfit of this peak was observed only for the rhombohedral model. It should be mentioned that the shape of this peak is likely affected by termination ripples from the truncation of the Fourier transform at Q_{max}. In this work, misfits of the rhombohedral model to the peaks at ~6.6 and 17.1 Å allow us to rule out this model in favor of both tetragonal and orthorhombic symmetries. The instrumental resolution employed in this work (Q_{max} = 25 Å^{-1}) was similar to those of Page (neutron scattering, Q_{max} = 30 Å^{-1}) and Petkov (X-ray scattering, Q_{max} = 28 Å^{-1}). Although never reported in previous PDF studies of sub-100 nm BTO nanocrystals, the coexistence of tetragonal and orthorhombic local symmetries in ultrafine BTO at room temperature has been suggested by a number of experimental studies on the basis of XRD,[12] Raman spectroscopy,[13] and dielectric[12,54] and calorimetric[13] data; theoretical work gave further support to these observations.[55] Specifically, the temperature of the orthorhombic-to-tetragonal phase transition has been found to increase upon decreasing the grain size. Frey and Payne demonstrated this transition temperature lies in the 20−40 °C range for an average grain size of ~35 nm.[13] Results from PDF analysis of XRD data presented in this work are in good agreement with the enhanced stability of the orthorhombic phase in BTO nanocrystals at room temperature. Finally, it should be noted that BTO nanocrystals employed by Page et al. and Petkov et al. were both prepared using a nonhydrolytic approach which utilizes benzyl alcohol as the solvent, whereas nanocrystals studied in this work are prepared through a hydrolytic approach in which the solvent is a mixture of n-butanol and 2-methoxypropanol. From this perspective, the possibility that different synthetic methods lead to nanocrystals exhibiting different local symmetry and surface chemistry deserves further and systematic investigation.

The superior fit of the *P4mm* model to the experimental data prompted us to investigate the evolution of the coherence of local tetragonal distortions with respect to reaction time and atom−atom pair distance. To this end, fits of this structural model to the experimental PDF of samples collected after a total reaction time ranging from 30 to 72 h were carried out from 8 to 28 Å in 4 Å increments;[56] for completeness, an additional fit including experimental data up to 48 Å was performed. The refinement strategy was the same as employed by Smith et al.[22] The fractional atomic coordinate z_{Ti} was refined while the positions of the oxygen atoms were held fixed at $(^1/_2,0,^1/_2)$ and $(^1/_2,^1/_2,0)$. This refinement strategy was based on the fact that X-ray scattering provides reliable positions for barium and titanium atoms. $BaCO_3$ was included as a secondary phase when modeling the PDF of samples collected at 36 and 72 h. The usual $(c/a - 1)$ metric was employed to assess the magnitude of the tetragonal distortion of the perovskite unit cell. PDFs calculated in the 1.5−20 Å distance range are shown in Figure 8 along with the experimental data. Goodness-of-fit indicators, refined structural parameters, and calculated distortion metrics are plotted in Figure 9. Inspection of these results shows that for the *P4mm* space group:

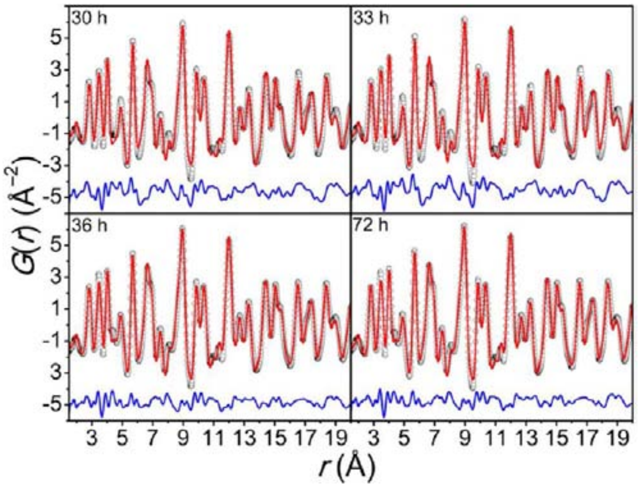

Figure 8. PDF analysis of synchrotron XRD data of BTO nanocrystals collected at 30, 33, 36, and 72 h. The experimental (○) and calculated (red line) PDF are shown for along with the difference curve (blue line); the latter has been offset for clarity. Fits were carried out in the 1.5−20 Å distance range using the *P4mm* space group.

- The fit to the experimental PDF of samples collected at 36 and 72 h is significantly better than to those of samples collected at 30 and 33 h, according to $R_{\mathrm{wp}}^{72\mathrm{h}} \approx R_{\mathrm{wp}}^{36\mathrm{h}} \ll R_{\mathrm{wp}}^{30\mathrm{h}}, R_{\mathrm{wp}}^{33\mathrm{h}}$ (Figure 9a).
- The best fit is obtained in the 1.5−16 Å distance range (∼4 unit cells), regardless of the total reaction time; the quality of the fit degrades progressively thereafter.
- The unit cell contracts as the total reaction time increases (Figure 9b), in agreement with results from Rietveld analysis. In addition, it expands as the fitting range increases; this occurs through an expansion of the lattice constant *a* and a contraction of *c* (Figure 9c).
- No significant variations in the value of the *c*/*a* ratio are observed upon increasing the total reaction time from 30 to 72 h (inset, Figure 9c). Furthermore, the unit cell becomes metrically more cubic upon increasing the fitting range as indicated by a decrease in the value of *c*/*a*.
- The average off-centering of the titanium atom along the polar direction *z* shows a slight decrease with increasing the reaction time, according to $z_{\mathrm{Ti}}^{30\mathrm{h}} > z_{\mathrm{Ti}}^{33\mathrm{h}} > z_{\mathrm{Ti}}^{36\mathrm{h}} \approx z_{\mathrm{Ti}}^{72\mathrm{h}}$ (Figure 9d); in addition, it increases significantly upon increasing the fitting range from 8 to 16 Å and remains relatively constant afterward.

The implications of these results for the description of the room-temperature crystal structure of sub-10 nm BTO nanocrystals are discussed as follows. In terms of the dependence of the structure with reaction time, R_{wp} values show that samples collected at 36 and 72 h exhibit significantly larger structural coherence than those collected at earlier stages, in agreement with Raman and Rietveld analysis data. This results from a notable decrease in the atomic positional disorder that occurs upon increasing the reaction time from 33 to 36 h, which suggests that the amorphous-to-crystalline phase transition is nearly completed at that point. The contraction of the unit cell and the decrease in the titanium off-centering with time reflect the increase in the size of crystalline domains within individual grains through the consumption of amorphous material; both phenomena are well-documented for BTO nanocrystals.[15,22,23] As demonstrated by *c*/*a* values higher than unity, and by the presence of a weak peak at ∼300 cm^{-1} in the Raman spectra of these samples, the decrease in atomic positional disorder leads to the development of non-centrosymmetric regions in which cooperative interactions between the local off-center displacements of the titanium atoms are maximized. Ultimately, this results in the development of tetragonal domains, i.e., ferroelectric nanoregions. The coherence length of these interactions appears to be on the order of 16 Å, or about four unit cells. This estimate is in good agreement with those previously reported in PDF investigations of the local structure of BTO nanocrystals exhibiting diameters in the 5−100 nm range.[15,20,22,23] The degradation of the quality of the fit of the tetragonal model and the observation that the perovskite unit cell becomes metrically more cubic upon increasing the fitting range further confirm that this local picture does not properly describe the average crystal structure. This trend is simply reflecting the increasing loss of coherence between pairs of atoms as these become farther apart; in particular, the local displacements of the titanium atoms become more randomly oriented resulting in an average cubic structure that shows no observable macroscopic polarization.[15,22]

Finally, we turn our attention to two results that are somewhat counterintuitive. First, it should be noted that *c*/*a* values extracted from PDF analysis are comparable to and even higher than those observed in bulk BTO, which are on the order of 1.011.[1] For example, in this work a *c*/*a* value of ∼1.013 was obtained for the sample collected at 72 h (fitting range: 1.5−20 Å). Similarly, Page et al. obtained values of ∼1.017 for ∼5 nm BTO nanocrystals (fitting range: 1−15 Å).[23] This is in striking contrast to the well-established knowledge that BTO nanoparticles exhibit *c*/*a* values lower than their bulk counterpart.[14,22,44] Furthermore, *c*/*a* values reported by Smith et al. upon PDF analysis over a 20 Å range showed an increase in *c*/*a* upon decreasing the nanocrystal size from 70 to 26 nm. In contrast, Rietveld analysis yielded the expected decrease of *c*/*a*.[22] These results can be reconciled by considering that the local crystal structure is less sensitive to disorder than the

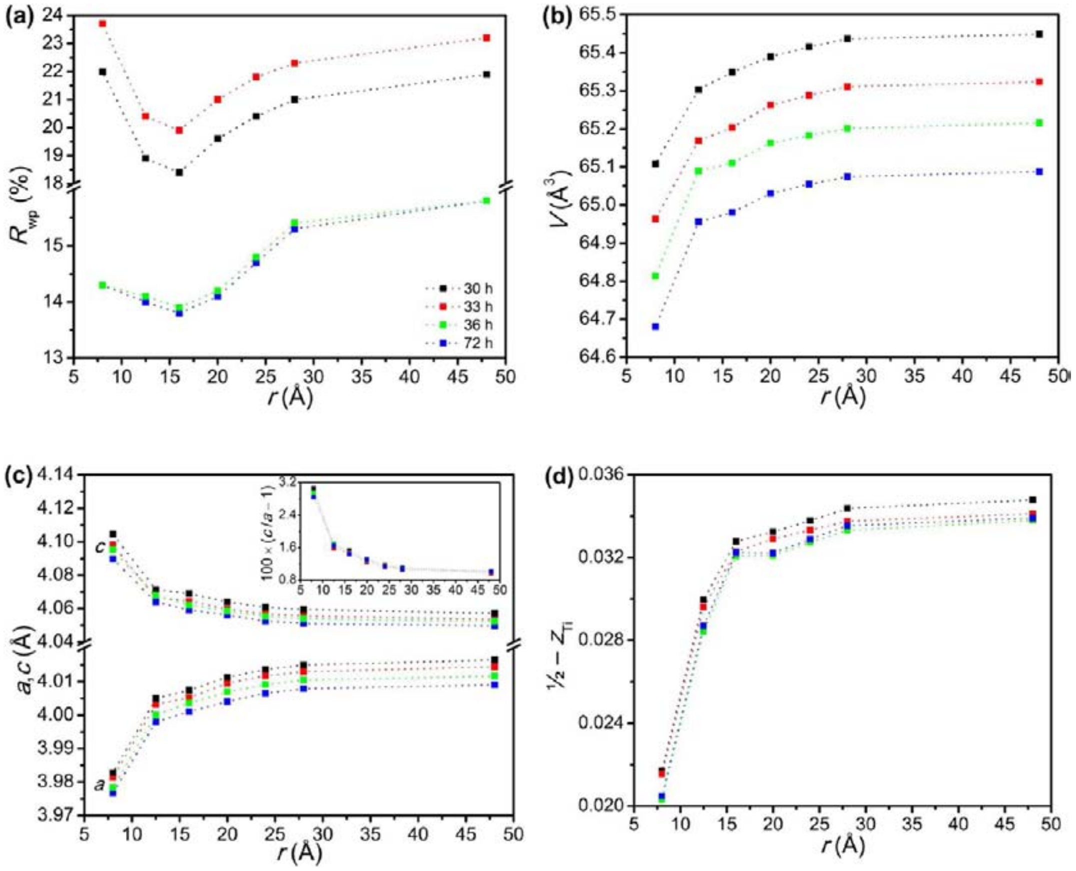

Figure 9. Results from PDF analysis of synchrotron XRD data of BTO nanocrystals collected at 30 (black squares), 33 (red squares), 36 (green squares), and 72 h (blue squares). (a) R_{wp} values. (b) Unit cell volume V. (c) Lattice constants a and c and values of the tetragonal distortion metric $100 \times (c/a - 1)$ (given in the inset). (d) Atomic fractional coordinate z_{Ti} given as $(^1/_2 - z_{Ti})$. Dotted lines are guides to the eye.

average structure, as proposed by Smith and co-workers. This decreased sensitivity leads to abnormally high values of c/a, particularly in low r ranges. A second counterintuitive result is the depressed titanium off-centering observed in the low r region and its subsequent increase upon increasing the fitting range; an identical trend was observed by Smith et al.[22] The increase in the titanium off-centering and the unit cell expansion observed upon increasing the fitting range are consistent with each other, as a larger off-centering of the titanium atom should lead to an enlarged unit cell. However, depressed local displacements of the titanium atom at low r are hard to reconcile with increased c/a ratios observed in this region, as in that case there is no structural basis for the elongation of the unit cell in the polar direction. It is remarkable, however, that z_{Ti} values obtained in this work are in good agreement with those extracted from PDF analysis of BTO nanocrystals of similar size.[20,23] Likewise, z_{Ti} values obtained for nanocrystals of different sizes consistently show an increase in the titanium atom off-centering upon reduction of the grain size.[22,23] Indeed, z_{Ti} values obtained in this work are comparable to those observed in bulk BTO.[1] All together, these observations demonstrate that although this metric is useful to capture the existence of local dipoles, it does not allow one to draw a fully consistent structural picture due to its inability to accurately reflect the presence of local disorder induced by spatial confinement of the system.[1] Therefore, the coupling between local off-center displacements of the titanium atoms in BTO nanocrystals should be modeled using geometrical patterns which are fundamentally different from those traditionally derived from single crystal and bulk BTO. Indeed, theoretical work by Fu and Bellaiche showed that the spatial arrangement of local dipoles in 5 nm BTO nanoparticles can adopt vortex-type patterns that lead to a vanishing macroscopic polarization.[57]

■ CONCLUSIONS

The structural evolution of sub-10 nm $BaTiO_3$ nanocrystals as they nucleate and grow from an amorphous metallorganic gel under ultrabenign conditions was investigated using a series of techniques that probe the atomic structure on different length and time scales. Upon the slow diffusion of water vapor into an alcohol solution of a bimetallic alkoxide $BaTi(OCH_2CHCH_3OCH_3)_6$ at room temperature, hydrolysis and polycondensation occurred and the solution gelled after ~8 h. The continued flow of water vapor over this gel resulted in the formation of $BaTiO_3$ nuclei within an amorphous metallorganic matrix at times as early as 12 h, as evidenced by TEM analysis. Gas−liquid rather than liquid−liquid hydrolysis and the use of a bimetallic alkoxide precursor are the keys to the formation of crystalline nuclei.[24] These 3−6 nm diameter nuclei continued to grow within the amorphous metallorganic matrix up until a reaction time of 27 h. During this growth stage, conventional and synchrotron XRD and Raman spectroscopy revealed a gradual increase in structural coherence and the simultaneous decrease in atomic positional disorder. After 30 h, discrete 9 nm diameter $BaTiO_3$ nanocrystals were obtained and the amorphous-to-crystalline phase transition quickly approached completion, as evidenced by TEM analysis. A significant increase in structural coherence was then confirmed by synchrotron XRD and Raman spectroscopy, which showed an increase in the intensity of coherent scattering and more intense vibrational bands, respectively.

The room-temperature crystal structure of the 9 nm nanocrystals appeared cubic to Rietveld analysis of synchrotron XRD data. However, the presence of non-centrosymmetric regions arising from the off centering of the titanium atoms was confirmed via Raman spectroscopy and PDF analysis; both techniques showed an increase in the coherence of these local off-center displacements upon approaching the completion of the amorphous-to-crystalline phase transition. The local structure of the acentric regions present in the fully grown nanocrystals after 72 h, specifically structural correlations within an individual unit cell *and* between two adjacent unit cells, are best described by a tetragonal *P*4*mm* symmetry. An orthorhombic *Amm*2 symmetry also provided an adequate structural description, demonstrating that the coexistence of both types of local symmetries is plausible. The coherence length of the local off-center displacements of the titanium atoms was found to be on the order of 16 Å, or about four unit cells. The presence of local dipoles whose average magnitude is comparable to that observed in bulk form suggests that a large amount of macroscopic polarization can be achieved in these nanocrystals if the long-range coherence of their ferroelectric coupling is restored. Crystal engineering and advanced theoretical modeling will be required to accomplish this technologically relevant goal.

■ ASSOCIATED CONTENT

Ⓢ Supporting Information

Thermograms corresponding to samples collected after total reaction times of 8, 15, 24, 30, 36, and 72 h; structure functions $S(Q)$ given as $Q[S(Q) - 1]$ for BTO nanocrystals obtained after total reaction times of 21, 24, 27, 30, 33, 36, and 72; TEM images of samples collected after total reaction times of 8, 15, 18, 21, 24, 33, and 36 h; synchrotron XRD patterns and Rietveld fits for samples collected after total reaction times of 21, 24, 33, 36, and 72 h; and Rietveld fits employing the *P*4*mm* space group for samples collected at 36 and 72 h. This material is available free of charge via the Internet at http://pubs.acs.org.

■ AUTHOR INFORMATION

Corresponding Author

brutchey@usc.edu

Notes

The authors declare no competing financial interest.

■ ACKNOWLEDGMENTS

This material is based on work supported by the Department of Energy Office of Basic Energy Sciences under Grant No. DE-FG02-11ER46826. The authors are thankful for the generous support provided by the Department of Chemistry and the Dornsife College of Letters, Arts, and Science at University of Southern California. They also thank Dr. Karena Chapman and Dr. Kevin Beyer from the Advanced Photon Source of Argonne National Laboratory for their assistance with the collection of synchrotron XRD data. Dr. Leopoldo Suescun from Cryssmat–Lab/DETEMA, Facultad de Quimica, Universidad de la Republica (Uruguay), Dr. Milen Gateshki from PANalytical (The Netherlands), and Dr. Efrain Rodriguez from NIST (USA) are also very gratefully acknowledged for their advice regarding the processing of synchrotron XRD data. Use of the Advanced Photon Source at Argonne National Laboratory was supported by the U.S. Department of Energy, Office of Science, Office of Basic Energy Sciences, under Contract No. DE-AC02-06CH11357. R.L.B. acknowledges the Research Corporation for Science Advancement for a Cottrell Scholar Award.

■ REFERENCES

(1) Kwei, G. H.; Lawson, A. C.; Billinge, S. J. L.; Cheong, S.-W. *J. Phys. Chem.* **1993**, *97*, 2368–2377.
(2) Cochran, W. *Adv. Phys.* **1960**, *9*, 387–423.
(3) Bersuker, I. B. *Phys. Lett.* **1966**, *20*, 589–590.
(4) Comes, R.; Lambert, M.; Guinier, A. *Solid State. Commun.* **1968**, *6*, 715–719.
(5) Wada, S.; Suzuki, T.; Osada, M.; Kakihana, M.; Noma, T. *Jpn. J. Appl. Phys.* **1998**, *37*, 5385–5393.
(6) Zalar, B.; Laguta, V. V.; Blinc, R. *Phys. Rev. Lett.* **2003**, *90*, 037601.
(7) Girshberg, Y.; Yacoby, Y. *Solid State. Commun.* **1997**, *103*, 425–430.
(8) Girshberg, Y.; Yacoby, Y. *J. Phys.: Condens. Matter* **1999**, *11*, 9807–9822.
(9) Pirc, R.; Blinc, R. *Phys. Rev. B* **2004**, *70*, 134107.
(10) Stern, E. A. *Phys. Rev. Lett.* **2004**, *93*, 037601.
(11) Zhang, Q.; Cagin, T.; Goddard, W. A. *Proc. Natl. Acad. Sci. U.S.A.* **2006**, *103*, 14695–14700.
(12) Arlt, G.; Hennings, D.; de With, G. *J. Appl. Phys.* **1985**, *58*, 1619–1625.
(13) Frey, M. H.; Payne, D. A. *Phys. Rev. B* **1996**, *54*, 3158–3168.
(14) Zhao, Z.; Buscaglia, V.; Viviani, M.; Buscaglia, M. T.; Mitoseriu, L.; Testino, A.; Nygren, M.; Johnsson, M.; Nanni, P. *Phys. Rev. B* **2004**, *70*, 024107.
(15) Petkov, V.; Buscaglia, V.; Buscaglia, M. T.; Zhao, Z.; Ren, Y. *Phys. Rev. B* **2008**, *78*, 054107.
(16) Junquera, J.; Ghosez, P. *Nature* **2003**, *422*, 506–509.
(17) Tenne, D. A.; Bruchhausen, A.; Lanzillotti-Kimura, N. D.; Fainstein, A.; Katiyar, R. S.; Cantarero, A.; Soukiassian, A.; Vaithyanathan, V.; Haeni, J. H.; Tian, W.; Schlom, D. G.; Choi, K. J.; Kim, D. M.; Eom, C. B.; Sun, H. P.; Pan, X. Q.; Li, Y. L.; Chen, L. Q.; Jia, Q. X.; Nakhmanson, S. M.; Rabe, K. M.; Xi, X. X. *Science* **2006**, *323*, 1614–1616.
(18) Uchino, K.; Sadanaga, E.; Hirose, T. *J. Am. Ceram. Soc.* **1989**, *72*, 1555–1558.
(19) Yashima, M.; Hoshina, T.; Ishimura, D.; Kobayashi, S.; Nakamura, W.; Tsurumi, T.; Wada, S. *J. Appl. Phys.* **2005**, *98*, 014313.
(20) Petkov, V.; Gateshki, M.; Niederberger, M.; Ren, Y. *Chem. Mater.* **2006**, *18*, 814–821.
(21) Shiratori, Y.; Pithan, C.; Dornseiffer, J.; Waser, R. *J. Raman Spectrosc.* **2007**, *38*, 1288–1299.
(22) Smith, M. B.; Page, K.; Siegrist, T.; Redmond, P. L.; Walter, E. C.; Seshadri, R.; Brus, L. E.; Steigerwald, M. L. *J. Am. Chem. Soc.* **2008**, *130*, 6955–6963.
(23) Page, K.; Proffen, T.; Niederberger, M.; Seshadri, R. *Chem. Mater.* **2010**, *22*, 4386–4391.
(24) Brutchey, R. L.; Morse, D. E. *Angew. Chem., Int. Ed.* **2006**, *45*, 6564–6566.
(25) Beier, C. W.; Cuevas, M. A.; Brutchey, R. L. *J. Mater. Chem.* **2010**, *20*, 5074–5079.
(26) Rabuffetti, F. A.; Brutchey, R. L. *Chem. Commun.* **2012**, *48*, 1437–1439.
(27) Rabuffetti, F. A.; Lee, J. S.; Brutchey, R. L. *Adv. Mater.* **2012**, *24*, 1434–1438.
(28) Rietveld, H. M. *Acta Crystallogr.* **1967**, *22*, 151–152.
(29) Rietveld, H. M. *J. Appl. Crystallogr.* **1969**, *2*, 65–71.
(30) Larson, A. C.; Von Dreele, R. B. *General Structure Analysis System (GSAS)*; Los Alamos National Laboratory, 2000.
(31) Thompson, P.; Cox, D. E.; Hastings, J. M. *J. Appl. Crystallogr.* **1987**, *20*, 79–83.

(32) Young, R. A. *The Rietveld Method*; Oxford University Press: New York, 1993.

(33) Petkov, V. *J. Appl. Crystallogr.* **1989**, *22*, 387−389.

(34) Farrow, C. L.; Juhas, P.; Liu, J. W.; Bryndin, D.; Bozin, E. S.; Bloch, J.; Proffen, T.; Billinge, S. J. L. *J. Phys.: Condens. Matter* **2007**, *19*, 335219.

(35) See footnote 45 in ref 20.

(36) Perry, C. H.; Hall, D. B. *Phys. Rev. Lett.* **1965**, *15*, 700−702.

(37) DiDomenico, M.; Wemple, S. H.; Porto, S. P. S. *Phys. Rev.* **1968**, *174*, 522−530.

(38) Scalabrin, A.; Chaves, A. S.; Shim, D. S.; Porto, S. P. S. *Phys. Stat. Sol. (b)* **1977**, *79*, 731−742.

(39) Busca, G.; Ramis, G.; Gallardo Amores, J. M.; Sanchez Escribano, V.; Piaggio, P. *J. Chem. Soc., Faraday Trans.* **1994**, *90*, 3181−3190.

(40) Busca, G.; Buscaglia, V.; Leoni, M.; Nanni, P. *Chem. Mater.* **1994**, *6*, 955−961.

(41) Robins, L. H.; Kaiser, D. L.; Rotter, L. D.; Schenck, P. K.; Stauf, G. T.; Rytz, D. *J. Appl. Phys.* **1994**, *76*, 7487−7498.

(42) Proust, C.; Husson, E.; Blondiaux, G.; Coutures, J. P. *J. Eur. Ceram. Soc.* **1994**, *14*, 215−219.

(43) Herman, R. G.; Bogdan, C. E.; Sommer, A. J.; Simpson, D. R. *Appl. Spectrosc.* **1987**, *41*, 437−440.

(44) Huang, T.-C.; Wang, M.-T.; Sheu, H.-S.; Hsieh, W.-F. *J. Phys.: Condens. Matter* **2007**, *19*, 476212.

(45) Antao, S. M.; Hassan, I. *Phys. Chem. Miner.* **2007**, *34*, 573−580.

(46) Ayyub, P.; Palkar, V. R.; Chattopadhyay, S.; Multani, M. *Phys. Rev. B* **1995**, *51*, 6135−6138.

(47) Ishikawa, K.; Uemori, T. *Phys. Rev. B* **1999**, *60*, 11841−11845.

(48) Tsunekawa, S.; Ishikawa, K.; Li, Z.-Q.; Kawazoe, Y.; Kasuya, A. *Phys. Rev. Lett.* **2000**, *85*, 3440−3443.

(49) Perebeinos, V.; Chan, S.-W.; Zhang, F. *Solid State. Commun.* **2002**, *123*, 295−297.

(50) Tsunekawa, S.; Ito, S.; Mori, T.; Ishikawa, K.; Li, Z.-Q.; Kawazoe, Y. *Phys. Rev. B* **2000**, *62*, 3065−3070.

(51) Pasciak, M.; Welberry, R. *Z. Kristallogr.* **2011**, *226*, 113−1125.

(52) Gilbert, B.; Huang, F.; Zhang, H.; Waychunas, G. A.; Banfield, J. F. *Science* **2004**, *305*, 651−654.

(53) The rhombohedral and orthorhombic crystal structures at −93 and −3 °C, respectively, were employed.

(54) Kanata, T.; Yoshikawa, T.; Kubota, K. *Solid State. Commun.* **1987**, *62*, 765−767.

(55) Fang, C.; Zhou, D. X.; Gong, S. P. *Mod. Phys. Lett.* **2010**, *24*, 2161−2170.

(56) The second data point was obtained after refinement in the 1.5−12.5 Å range.

(57) Fu, H.; Bellaiche, L. *Phys. Rev. Lett.* **2003**, *91*, 257601.